Magnesium Technology 2011
Edited by: Wim H. Sillekens, Sean R. Agnew, Neale R. Neelameggham, and Suveen N. Mathaudhu
TMS (The Minerals, Metals & Materials Society), 2011

Magnesium Technology 2011

High-Temperature Alloys; High-Strength Alloys; Precipitation

Session Chairs:

Alan A. Luo
(General Motors, USA)
Alok Singh
(National Institute for Materials Science, Japan)

Magnesium Technology 2011
Edited by: Wim H. Sillekens, Sean R. Agnew, Neale R. Neelameggham, and Suveen N. Mathaudhu
TMS (The Minerals, Metals & Materials Society), 2011

Creep and elemental partitioning behavior of Mg-Al-Ca-Sn alloys with the addition of Sr

Jessica R. TerBush[1,2], Olivia H. Chen[1], J. Wayne Jones[1] and Tresa M. Pollock[1,3]
[1] Materials Science and Engineering, University of Michigan; 2300 Hayward St, Ann Arbor, MI 48109, USA
[2] Department of Materials Engineering, Monash University; Clayton, VIC 3800, Australia
[3] Materials Department, University of California; Santa Barbara, CA 93106, USA

Keywords: Creep; Solute Strengthening; Precipitation; Elemental Partitioning

Abstract

The partitioning of elements during solidification can strongly affect precipitation and solute strengthening during creep, especially in alloys where creep is controlled by viscous glide of dislocations. Elemental partitioning during solidification and its influence on creep behavior has been examined for Mg-6.5Al-2.25Ca-0.8Sn with and without 0.25wt% Sr additions. The alloy containing Sr experienced increased partitioning of Al and Ca to the α-Mg phase. However, the creep behavior in compression at 110 MPa and 180°C was not significantly different from that of the alloy without Sr. These observations are discussed in terms of current models for solid solution and precipitation strengthening. In addition, it was determined that the elemental partitioning profiles of permanent mold cast specimens were representative of the grain interiors of die-cast specimens. The partitioning profiles may be less representative for interdendritic regions of the microstructure, however.

Introduction

In the automotive industry, the use of magnesium alloys is aiding efforts to reduce vehicle mass. Many new applications are in automotive powertrain components that experience elevated temperatures, which require alloys with good creep resistance above 150°C [1]. Cast alloys are generally used for powertrain applications, and creep properties in these materials are sensitive to both the solidification behavior and therefore the casting process parameters. These alloys are usually used in the as-cast state, making it important to understand the elemental partitioning that occurs during solidification, as it can ultimately affect high temperature strengthening mechanisms.

Solute redistribution occurs during solidification, resulting in compositional variation from dendrite centers to interdendritic regions [2, 3]. In Mg alloys, this means that the α-Mg that forms at the beginning of solidification (i.e. in the cell interiors) will have a lower solute concentration than the solid that forms in the near-interdendritic regions later in solidification. Solute enrichment in the interdendritic region at the end of solidification leads to the precipitation of intermetallic phases. If no appreciable back diffusion occurs during solidification, the solute will remain inhomogeneously distributed across the microstructure [3]. In the case of no back diffusion in the solid and perfect mixing in the liquid, the Scheil equation is often used to describe the elemental distribution under non-equilibrium conditions:

$$C_s = kC_0(1-f_s)^{(k-1)} \quad (1).$$

Here, C_s is the concentration of solute in the solid, C_0 is the bulk average concentration, f_s is the fraction solid and k is the partitioning coefficient, which is also defined as (C_s / C_L) where C_L is the concentration of solute in the liquid [4, 5]. Elements with $k > 1$ will preferentially segregate to the dendrite centers, while those with $k < 1$ will segregate to the interdendritic region during solidification. Elements with $k \approx 1$ will not segregate strongly.

Mg-Al-Ca-based alloys have received considerable attention for powertrain applications [1, 6-14]. In our previous work, elemental partitioning has been examined for four Mg-Al-Ca-based alloys [15, 16] where it was discovered that MRI230D (Mg-6.5Al-2.25Ca-0.25Sr-0.8Sn) had significantly increased partitioning of Al and Ca to the α-Mg phase during solidification. It was hypothesized that the presence of Sn in this alloy led to the increased partitioning compared to the other alloys studied, which did not contain Sn. This motivated an investigation of elemental partitioning in quaternary Mg-5Al-3Ca-xSn alloys, described elsewhere [17]. The increased partitioning to the α-Mg observed in MRI230D could not be explained by Sn additions alone. However, MRI230D also contains 0.25 wt% Sr, which was reported to affect the elemental partitioning during solidification of a Mg-5Al-3(Ca,Sr) alloy [8]. Thus, an investigation on the effect of Sr additions on elemental partitioning during solidification has been conducted for this Mg-Al-Ca-Sn alloy.

Of particular interest is how differences in elemental partitioning translate to differences in creep resistance. For example, die-cast MRI153M (Mg-8Al-1Ca-0.25Sr), which has higher Al partitioning and lower Ca partitioning to the α-Mg phase, is less creep resistant than MRI230D and AXJ530 when tested at 110 MPa and temperatures between 100 and 180°C [18]. However, different nominal compositions in these alloys complicates the analysis. Increased solute in the α-Mg can potentially increase solute and precipitation strengthening at elevated temperatures [10], although supersaturation of solute (e.g. Al) has also been linked to decreased creep resistance in some alloys, especially where β-$Mg_{17}Al_{12}$ precipitates form during high temperature exposure [19, 20].

The current investigation examines the elemental partitioning and creep behavior for an Mg-6.5Al-2.5Ca-0.8Sn alloy with and without additions of Sr. The effect of systematic additions of Sn

on partitioning of Ca and Al and creep behavior has also been examined.

Experimental Procedure

An alloy with nominal composition of Mg-6.5Al-2.25Ca-0.8Sn (in wt%) was prepared from a master alloy of Mg-4Al-4Ca with additions of pure (99.9%) Mg ingot, (99.5%) Al lump and (99.99%) Sn ingot. The starting materials were melted in a low-carbon steel crucible under a cover gas of 1% SF_6 in Ar using an induction heater. The melt was stirred for several minutes prior to pouring onto an unheated steel plate. A cooling rate of several degrees Celsius per second was obtained for 25 g samples.

Similar casting conditions were used to prepare 25g samples of Mg-6.5Al-2.25Ca-0.25Sr-0.8Sn (MRI230D). For this alloy, the starting material consisted of die-cast specimens of MRI230D, made from original ingots produced by Dead Sea Magnesium. The starting material (die-cast specimens) had an average cell size of ~11 μm, while the slower cooling rate in the current study produced an average cell size of ~20 μm, which facilitated determination of composition profiles.

The as-cast samples for both alloys were sectioned and cold mounted in resin and prepared using standard metallographic procedures. The final polishing step consisted of 0.25 μm diamond paste on a neoprene pad with ethanol lubrication. Samples were not etched prior to microstructural examination in a Philips XL30 SEM operating in backscattered electron (BSE) mode.

Elemental partitioning in as-cast alloys was investigated using a Cameca SX100 electron microprobe. The same sample preparation steps used for SEM analysis were used for the microprobe studies. WDS standards consisted of pure metal and mineral samples, with one exception. The Mg standard used was a sample of Mg-4wt%Al that had been homogenized for 26 days at 400°C. Compositional mapping used a procedure similar to that of Flemings et al. [21], Gungor [22], Tin et al. [23] and Huang et al. [24]. Area scans consisting of at least 400 points were collected from multiple regions of the sample, with an average step size of 10 μm between each point. A voltage of 20 kV and beam current of 15 nA were used for each scan, resulting in an electron beam spot size of approximately 2 μm. Only points with total concentrations between 99 and 101 wt% were used for subsequent analysis. Totals outside this range could be caused by sampling more than one phase simultaneously or by oxide films or inclusions. The resulting data was sorted according to decreasing Mg concentration as described in our previous work [15-17].

Compressive creep tests were conducted on parallelepiped specimens measuring approximately 4x4x8 mm^3 that were sectioned from the induction melted samples. Specimens were ground using 400 grit SiC paper with water lubrication until all sides were flat and parallel. For creep testing, a compression cage was inserted into an Arc-weld constant-load tensile creep frame fitted with a clam-shell furnace. An LVDT attached to an extensometer was used to monitor strain, while temperature was monitored with a K-type thermocouple in contact with the specimen. Testing was carried out at 110 MPa at a temperature of 180°C. Tests were generally interrupted after strain accumulation of 0.1, and specimens were cooled to room temperature under load.

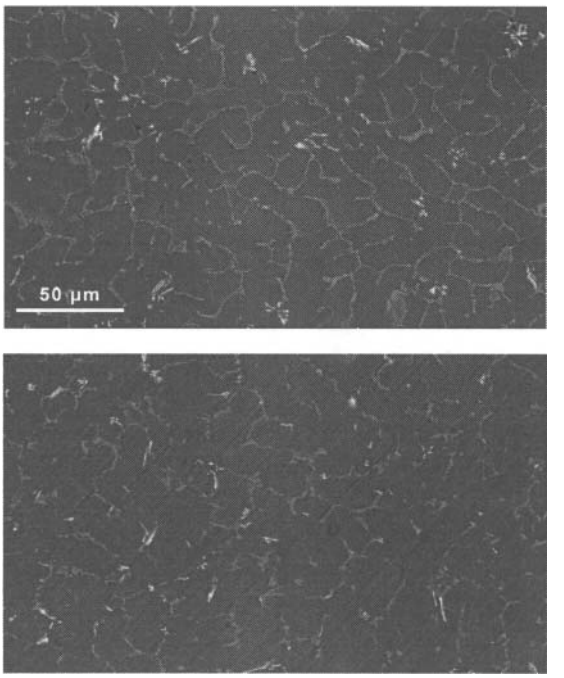

Figure 1 - SEM (BSE) images of the as-cast microstructure of a) MRI230D and b) Mg-6.5Al-2.25Ca-0.8Sn.

For selected crept specimens, dislocation substructures were examined after creep using TEM. Discs 3 mm in diameter were punched from slices made perpendicular to the loading direction, and then thinned by hand to 0.11-0.12 mm thickness. Final thinning to electron transparency was done via twin-jet polishing using a solution of 8 vol% perchloric acid in methanol at -30°C. A Philips CM12 transmission electron microscope was used for the investigation, with an operating voltage of 120 kV.

Results and Discussion

The as-cast microstructures for the alloy with and without Sr are shown in Fig. 1, and are very similar morphologically. The major phase is α-Mg, surrounded by a eutectic microstructure consisting mainly of C36 $(Mg,Al)_2Ca$ and α-Mg. A low volume fraction of a Sn-containing phase, likely CaMgSn ($Ca_{2-x}Mg_xSn$) [25, 26], is also observed in both alloys. A low volume fraction of a Sr-rich phase is also present in the Sr-containing MRI230D. Scheil calculations using the Pandat thermodynamic database predict that β-$Mg_{17}Al_{12}$ will also be present in both alloys, with a higher volume fraction expected in the quaternary Mg-6.5Al-2.25Ca-0.8Sn alloy.

In Fig. 2, the elemental partitioning behavior during solidification is compared for the two alloys for both Al and Ca. The curves shown in this figure are least-mean-square (LMS) fits to the data, presented for ease of comparison. Although not shown here, some scatter does exist in the experimental data, a consequence of the data sorting method used [27]. Based on the shape of the partitioning profiles, MRI230D has higher Al and Ca partitioning to the α-Mg phase than the quaternary alloy without Sr. The Al and Ca partitioning curves are fairly similar for both alloys at the start of solidification and near the end, with the greatest differences observed for fractions solid between 0.5 and 0.8. This suggests that Sr additions may cause differences in the local

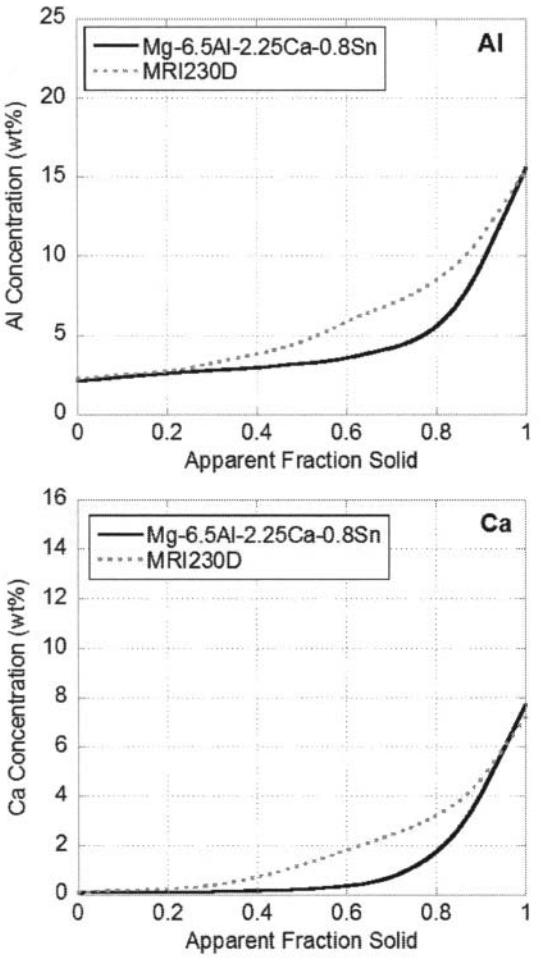

Figure 3 - Comparison of elemental partitioning curves for MRI230D and Mg-6.5Al-2.25Ca-0.8Sn: a) Al and b) Ca profiles.

Table I - Calculated partitioning coefficients (k)

Alloy	Mg	Al	Ca	Sn	Sr
AXJ530 [31]	1.03	0.38	0.06	-	*
Mg-5Al-3Ca-0.75Sn	1.08 ±0.03	0.28 ±0.05	0.09 ±0.03	0.05 ±0.02	-
Mg-6.5Al-2.25Ca-0.8Sn	1.07 ±0.03	0.32 ±0.05	0.06 ±0.03	0.07 ±0.04	-
Mg-6.5Al-2.25Ca-0.25Sr	1.14 ±0.03	0.27 ±0.04	0.02 ±0.01	-	0.04 ±0.03
Mg-6.5Al-2.25Ca-0.8Sr	1.11 ±0.03	0.30 ±0.05	0.03 ±0.02	-	0.05 ±0.03
MRI230D [16]	1.10 ±0.02	0.42 ±0.08	0.17 ±0.07	0.08 ±0.04	0.08 ±0.05

* Not reported

concentration, especially in the near-interdendritic region of the microstructure.

To quantify this difference, a Scheil equation has been fit to the experimental data for 10-60% solid. The partitioning coefficients calculated are listed in Table I. For comparison, calculated coefficients are also included for AXJ530 (Mg-5Al-3Ca-0.15Sr), Mg-5Al-3Ca-0.75Sn, Mg-6.5Al-2.25Ca-0.25Sr and Mg-6.5Al-2.25Ca-0.8Sr. MRI230D has the highest partitioning of Al and Ca to the α-Mg phase. Comparing the coefficients for AXJ530 and Mg-5Al-3Ca-0.75Sn, Sn additions appear to increase Ca partitioning to the α-Mg phase. However, the influence of Sn on Al partitioning is less clear; the Mg-5Al-3Ca-0.75Sn alloy has lower Al partitioning to the α-Mg phase than AXJ530, while Mg-6.5Al-2.25Ca-0.8Sn has increased Al partitioning compared to the Mg-6.5Al-2.25Ca-0.8Sr alloy. From comparison of the Sr-containing quaternary alloys, Sr appears to increase Al partitioning to the α-Mg, but does not affect Ca partitioning. Thus, the increased Al and Ca partitioning to the α-Mg phase observed in MRI230D is likely due to the combination of Sn and Sr present in this alloy.

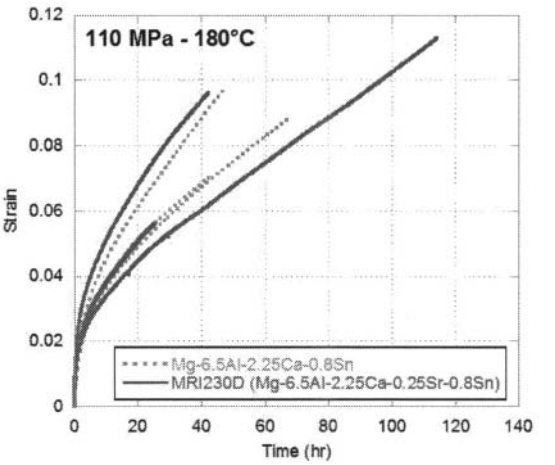

Figure 2 - Compressive creep curves for specimens tested at 110 MPa and 180°C.

Table II - Compressive creep rates at 110 MPa and 180°C

Alloy	Minimum Creep Rate (x 10^{-7} s^{-1})	Avg. Minimum Creep Rate (x 10^{-7} s^{-1})
Mg-6.5Al-2.25Ca-0.8Sn	3.30	2.51
	2.12	
	2.10	
MRI230D	1.97	2.51
	3.01	
	2.54	

To determine how the difference in partitioning with Sr addition affects creep resistance, compressive creep tests were performed at 110 MPa and 180°C, Fig. 3, and minimum creep rates are listed in Table II. The average minimum creep rate for both MRI230D and Mg-6.5Al-2.25Ca-0.8Sn was 2.51×10^{-7} s^{-1}, indicating that Sr does not affect creep resistance in Mg-Al-Ca alloys that also contain Sn. In contrast, minor additions of Sr have been reported to increase creep resistance in Mg-Al-Ca alloys without Sn additions [6, 11, 28]. Further experiments are needed to fully understand the role of Sr in creep resistance.

The dislocation substructures were examined for the crept samples. An example is shown in Fig. 4 for MRI230D. The

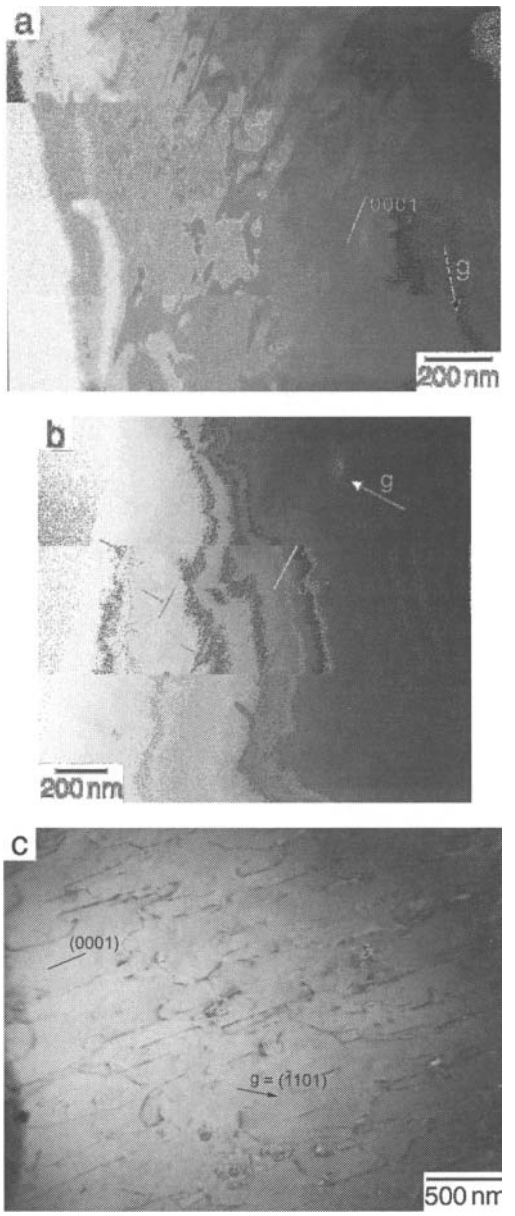

Figure 4 - BF TEM images of a compressively crept sample of MRI230D, taken from a ZA of $[11\bar{2}0]$. a) g = $(1\bar{1}01)$ and b) g = (0002). Precipitates are indicated by the small arrows. c) Crept sample of die-cast MRI230D [18], tested in tension at 110 MPa and 180°C.

Table I - Calculated values of (e^2c/D)

Alloy	Al	Ca	Al + Ca
Mg-6.5Al-2.25Ca-0.8Sn	1.23×10^{12}	1.66×10^{12}	2.89×10^{12}
MRI230D	1.63×10^{12}	6.66×10^{12}	8.29×10^{12}

images were taken from a zone axis of $[11\bar{2}0]$. The majority of the dislocations visible have been identified as basal <a> dislocations, which are invisible under the conditions used in Fig.

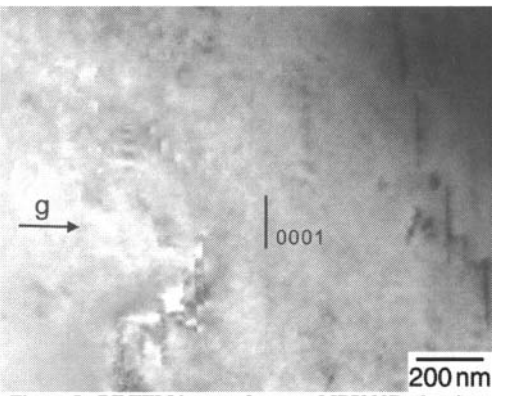

Figure 5 - BF TEM image of as-cast MRI230D, showing precipitates present in the α-Mg. ZA = $[11\bar{2}0]$ and g = (0002).

4b. The small arrows in Fig. 4b indicate precipitates in the α-Mg matrix. Similar dislocation substructures were identified previously in die-cast samples of MRI230D tested in tension under similar stress and temperature conditions [18], Fig. 4c, with a limited number of non-basal <a> and <c+a> dislocations also present. As in the die-cast samples, viscous glide of basal <a> dislocations was once again identified as the major deformation mechanism during creep.

For alloys where creep is controlled by viscous glide of dislocations, creep resistance can be improved by inhibiting dislocation motion through the α-Mg. This can be accomplished by increasing solute in the matrix, or by the formation of precipitate phases that interact with the moving dislocations. For the alloys currently under investigation, both mechanisms are likely active. Mohamed and Langdon [29] developed an expression relating the creep rate ($\dot{\varepsilon}$) in solute strengthened alloys to solute concentration (c), atomic misfit of the solute atom (e), and diffusivity ($\tilde{D}$):

$$\dot{\varepsilon} \approx \frac{\pi(1-\nu)kT\tilde{D}}{6e^2cb^5G}\left(\frac{\sigma}{G}\right)^3 \qquad (2),$$

Where ν is Poisson's ratio, k is Boltzmann's constant, σ is the applied stress, T is the absolute temperature, b is the Burgers vector and G is the shear modulus. A large contribution from the alloy-sensitive ($e^2c/\tilde{D}$) term would result in a low creep rate, assuming all other terms are similar for the alloys. The average concentration measured using the electron microprobe was determined for solid fractions between 0 and 0.7 and used for c in the calculations. The average Al concentration was 2.66 at% for Mg-6.5Al-2.25Ca-0.8Sn and 3.51 at% for MRI230D, and Ca concentrations of 0.12 at% and 0.48 at%, respectively. For e, values of 0.124 and 0.204 were used for Al and Ca, respectively. The diffusion coefficient in these complex alloys is not well known. Approximating the diffusivity as 3.32×10^{-16} cm^2/s at 180°C [30] for Al in Mg, and as one order of magnitude less for Ca ($\sim3\times10^{-17}$ cm^2/s), the calculated values of ($e^2c/\tilde{D}$) are listed in Table III for both alloys. As would be expected from the higher average concentrations of solute in the α-Mg, the model predicts that MRI230D should have the lower creep rate. However, as described earlier, this was not observed experimentally.

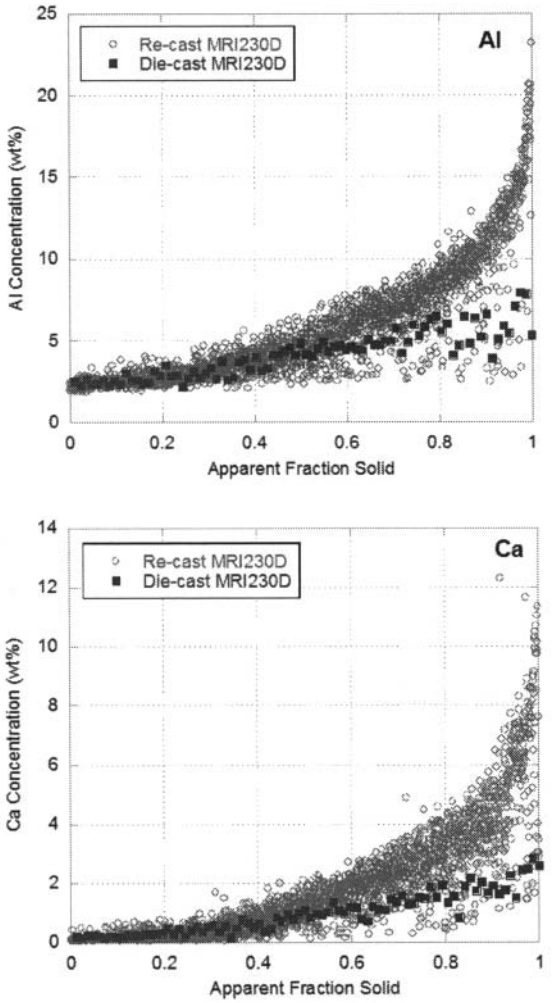

Figure 4 - Comparison of the elemental partitioning curves for die-cast and permanent-mold-type specimens of MRI230D: a) Al and b) Ca profiles.

In the previous calculation, it was assumed that the entire measured concentration of Al and Ca was in the form of solute in the Mg matrix. However, the electron microprobe does not distinguish between solute and nanoscale precipitates when measuring elemental concentrations. As shown in Fig. 5 for MRI230D, precipitates are present even in the as-cast condition. These precipitates lie parallel to the basal plane of the α-Mg matrix, and are likely C15 Al_2Ca as observed in other Mg-Al-Ca alloys, e.g. AXJ530 [10]. These precipitates are also present in the crept alloys, Fig. 4b. According to Pandat equilibrium calculations, similar volume fractions of the C15 phase are expected for both MRI230D and Mg-6.5Al-2.25Ca-0.8Sn. Although not very effective obstacles for basal dislocations, these precipitates are fairly effective obstacles for non-basal dislocations [10]. It has been suggested that non-basal dislocations in the near-grain boundary region account for the localized damage that occurs after the minimum creep rate is reached in samples of permanent mold cast AXJ530 [31]. Moreno et al. [32] and Mori et al. [33] have both suggested that the composition of the near-boundary region may have significant effect on creep resistance of Mg alloys. The increased Al and Ca concentration measured in this region of the microstructure in the current investigation suggests that further study may be needed of the near-boundary region of the α-Mg.

Many automotive applications involve components that are high pressure die cast, and EMPA area and line scans were also conducted on a die-cast sample of MRI230D to determine if segregation was comparable to that observed in permanent mold cast alloys reported here or in previous studies [15-17]. Step sizes of 3-5 μm were used, and the line scans extended across several cells. The die-cast material had an average cell size of ~10 μm, which increased the frequency of sampling multiple phases when both the cell interiors and neighboring interdendritic regions were scanned simultaneously. This was especially true in the near-interdendritic region, and in turn lead to a large number of points that fell outside the acceptable composition range (99-101 total wt%). As before, these points were disregarded during the subsequent analysis. However, enough points were generated for a rough comparison to the segregation behavior of induction melted samples.

Elemental partitioning profiles are shown for both casting conditions in Fig. 6. These profiles show the experimental data and the inherent scatter. The Al and Ca profiles in the die cast material overlap with those in the induction melted samples at apparent fractions solid of approximately 0.5 or less. Thus, the partitioning data presented earlier for the induction melted samples are also representative of the grain interiors of die-cast specimens of the same alloy. However, greater differences may exist in the near-interdendritic region, since lower Al and Ca concentrations were measured in this region for the die-cast specimen. Again, this analysis was somewhat complicated by the small cell size of the die-cast alloys; the electron microprobe technique employed in this study is not ideal for materials with smaller microstructural features (e.g. die-cast alloys). Further investigation is needed, perhaps using higher resolution STEM techniques, to determine whether these differences in local composition in the near-interdendritic region are an artifact of the measurement technique used or reflect elemental partitioning variations with casting process and/or cooling rate.

Summary

1. Increased Al and Ca solute are present in the α-Mg phase of MRI230D and this is attributed to the combined influence of Sr and Sn. Compared with the quaternary alloy without Sr, the largest difference in the Al and Ca concentration profile of MRI230D was observed in the near-interdendritic region.

2. Sr additions do not significantly affect creep resistance in Mg-Al-Ca alloys that also contain Sn, although improvements have been reported in Mg-Al-Ca alloys without Sn. Further study is necessary to mechanistically explain the effect of Sr on creep resistance.

3. Elemental partitioning profiles measured for more slowly cooled permanent-mold cast specimens are representative of the profiles for die-cast specimens for fractions solid of ~0.5 or less (i.e. the grain interiors).

Acknowledgements

The authors acknowledge the support of the National Science Foundation FRG, Grants No. F015408 and DMR-0309468. We also thank B.R. Powell (General Motors), C. Torbet (UC – Santa Barbara) R.R. Adharapurapu (University of Michigan) and C. Henderson (University of Michigan EMAL) for their advice and assistance.

References

[1] A. A. Luo, International Materials Reviews 49 (2004) 13-30.

[2] Y. M. Won, B. G. Thomas, Metallurgical and Materials Transactions 32A (2001) 1755-1767.

[3] D. A. Porter, K. E. Easterling, Phase Transformations in Metals and Alloys, Nelson Thornes Ltd, Cheltenham, 1992, pp. 185-262.

[4] H. D. Brody, M. C. Flemings, Transactions of the Metallurgical Society of AIME 236 (1966) 615-624.

[5] T. F. Bower, H. D. Brody, M. C. Flemings, Transactions of the Metallurgical Society of AIME 236 (1966) 624-634.

[6] A. A. Luo, M. P. Balogh, B. R. Powell, Metallurgical and Materials Transactions 33A (2002) 567-574.

[7] S. M. Zhu, B. L. Mordike, J. F. Nie, Materials Science and Engineering A 483-484 (2008) 583-586.

[8] A. Suzuki, N. D. Saddock, L. Riester, E. Lara-Curzio, J. W. Jones, T. M. Pollock, Metallurgical and Materials Transactions A 38A (2007) 420-427.

[9] A. Suzuki, N. D. Saddock, J. R. TerBush, B. R. Powell, J. W. Jones, T. M. Pollock, SAE Technical Paper 2007-01-1025, SAE International, Detroit, MI, 2007.

[10] A. Suzuki, N. D. Saddock, J. R. TerBush, B. R. Powell, J. W. Jones, T. M. Pollock, Metallurgical and Materials Transactions A 39A (2008) 696-702.

[11] N. D. Saddock, A. Suzuki, J. R. TerBush, J. W. Jones, T. M. Pollock, J. E. Zindel, J. E. Allison, SAE Technical Paper 2007-01-1027, SAE International, Detroit, MI, 2007.

[12] S. M. Zhu, B. L. Mordike, J. F. Nie, Metallurgical and Materials Transactions A 37A (2006) 1221-1229.

[13] Y. Terada, N. Ishimatsu, T. Sato, Mat Trans 48 (2007) 2329-2335.

[14] J. A. Hines, R. C. McCune, J. E. Allison, B. R. Powell, L. J. Ouimet, W. L. Miller, R. Beals, L. Kopka, P. P. Ried, SAE Technical Paper 2006-01-0522, SAE International, Detroit, MI, 2006.

[15] J. R. TerBush, R. R. Adharapurapu, J. W. Jones, T. M. Pollock, in: E. A. Nyberg, S. R. Agnew, N. R. Neelameggham, M. O. Pekguleryuz (Eds.), Magnesium Technology 2009, TMS, San Francisco, CA, 2009, pp. 161-165.

[16] J. R. TerBush, N. D. Saddock, J. W. Jones, T. M. Pollock, Metallurgical and Materials Transactions A 41 (2010) 2435-2442.

[17] J. R. TerBush, O. H. Chen, J. W. Jones, T. M. Pollock, in: S. R. Agnew, E. Nyberg, W. Sillekens, N. R. Neelameggham (Eds.), Magnesium Technology 2010, TMS, Seattle, WA, 2010, pp. 607-611.

[18] J. R. TerBush, A. Suzuki, N. D. Saddock, J. W. Jones, T. M. Pollock, Scripta Materialia 58 (2008) 914-917.

[19] S. M. Zhu, M. A. Gibson, J. F. Nie, M. A. Easton, T. B. Abbott, Scripta Materialia 58 (2008) 477-480.

[20] M. S. Dargusch, S. M. Zhu, J. F. Nie, G. L. Dunlop, Scripta Materialia 60 (2009) 116-119.

[21] M. C. Flemings, D. R. Poirier, R. V. Barone, H. D. Brody, Journal of the Iron and Steel Institute 208 (1970) 371-381.

[22] M. Gungor, Metallurgical Transactions A 20 (1989) 2529-2533.

[23] S. Tin, T. M. Pollock, W. Murphy, Metallurgical and Materials Transactions A 32 (2001) 1743-1753.

[24] S. C. Huang, L. Peluso, D. Backman, in: W. H. Hofmeister, J. R. Rogers, N. B. Singh, S. P. Marsh, P. W. Vorhees (Eds.), Solidification, TMS, 1999, pp. 163-172.

[25] A. Kozlov, M. Ohno, T. Abu Leil, N. Hort, K. U. Kainer, R. Schmid-Fetzer, Intermetallics 16 (2008) 316-321.

[26] A. Kozlov, M. Ohno, R. Arroyave, Z. K. Liu, R. Schmid-Fetzer, Intermetallics 16 (2008) 299-315.

[27] M. Ganesan, D. Dye, P. D. Lee, Metallurgical and Materials Transactions 36A (2005) 2191-2204.

[28] B. R. Powell, V. Rezhets, A. A. Luo, B. L. Tiwari, US Patent 6,264,763, 2001.

[29] F. A. Mohamed, T. G. Langdon, Acta Metall. 22 (1974) 779-788.

[30] G. Moreau, J. A. Cornet, D. Calais, Journal of Nuclear Materials 38 (1971) 197-202.

[31] N. D. Saddock, PhD Thesis, University of Michigan, Ann Arbor, MI, 2007.

[32] I. P. Moreno, T. K. Nandy, J. W. Jones, J. E. Allison, T. M. Pollock, Scripta Materialia 48 (2003) 1029-1034.

[33] Y. Mori, Y. Terada, T. Sato, Materials Transactions 46 (2005) 1747-1752.